Applied Surface Science 669 (2024) 160578

Contents lists available at ScienceDirect

Applied Surface Science

journal homepage: www.elsevier.com/locate/apsusc

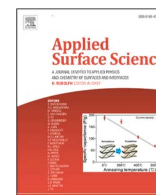

Full Length Article

Detailed work function and structural investigations of layered MoO_3 onto SiO_2 and MoS_2 in air

Saeed Sovizi [a], Sergio Tosoni [b], Tomasz Zdunek [a], Robert Szoszkiewicz [a,*]

[a] Faculty of Chemistry, Biological and Chemical Research Centre, University of Warsaw, Żwirki i Wigury 101, 02-089 Warsaw, Poland
[b] Dipartimento di Scienza dei Materiali, Università di Milano-Bicocca, via Roberto Cozzi 55, 20125 Milan, Italy

ARTICLE INFO

Keywords:
Molybdenum disulfide
Molybdenum trioxide
Work function
Atomic force microscopy
Kelvin-probe force microscopy

ABSTRACT

MoS_2, its oxides and heterostructures are increasingly utilized in nanoscale opto-electronics and catalysis, where electrical properties such as work function (WF) affect their performance. Herein, a detailed study of the thickness-dependent work function in the case of thermally produced layered Mo oxides onto SiO_2 and MoS_2 substrates in air is presented. First, the effects of typical contaminants on the mechanically exfoliated MoS_2 substrates are investigated. Then, high resolution structural characterization by atomic force microscopy supported by X-ray photoelectron spectroscopy shows that thermal MoS_2 oxidation in humid air produces layered amorphous MoO_3 with nano-crystallites. Kelvin-probe force microscopy analysis shows that the first MoO_3 layer on both substrates is negatively charged and that the MoO_3 work function depends on the oxide thickness. The thickness-dependent WF is explained by presence of screened electric field at the MoO_3/substrate interface. The negative doping to MoO_3 by the studied substrates is confirmed through density functional theory simulations. Moreover, an electrical device from amorphous MoO_3 monolayer onto MoS_2 is built and shows rectification behavior due to p-type doping of the MoS_2 by the oxide layer. Overall, this study provides an insight to understand and manipulate electrical properties of MoO_3 and MoO_3/MoS_2 heterostructures in various devices.

1. Introduction

As a member of the transition metal dichalcogenides family, MoS_2 has attracted particular attention due to its fascinating properties including, but not limited to, high surface-to-volume ratio, high electron mobility in its semiconducting 2H phase and a tunable bandgap. As a consequence, layered semiconducting 2H MoS_2 has been already synthesized with various methods and utilized in energy harvesting, opto-electronics and sensing [1–4]. While 2H MoS_2 is chemically inert in air at room temperature it starts to oxidize above 300 °C to produce volatile oxides as well as surface etch pits [5,6]. Water and its vapors have been found to promote oxidation and accumulation of surface bound Mo oxides, mostly in the form of MoO_3 [6,7]. Besides possible adverse effects of the MoS_2 oxidation for the MoS_2-based devices, deliberate p-type doping through oxidation is expected to find applications in nano- and opto-electronics due to creation of local p-n junctions [8,9]. Such MoS_2 p-type doping has been already observed as originating from MoO_x formed on the samples either through soft O_2 plasma treatment [5,10,11] or incomplete sulfurization of pre-deposited Mo or MoO_x films [12,13].

Knowing an appropriate value of the work function (WF) is critical for understanding the p-n junctions as well as any related metal–semiconductor junctions. Work function affects as well an electron transfer between the reactants/intermediates on the semiconductor surfaces with catalytic properties [14–16]. As a result, studying the work function of MoS_2, MoO_3 and their heterostructures paves the way for further extensive research on electronic devices and catalysis [17].

Typically, photoemission spectroscopy (PES) and Kelvin-probe force microscopy (KPFM) methods have been utilized to measure the work function. PES measurements are usually performed in vacuum and have energy resolution of 400 meV or less and spatial resolution of 1 μm, which has been recently reduced to 20 nm depending on the analyzer and photon flux density [18–20]. KPFM is an atomic force microscopy (AFM) technique used for simultaneous measurements of local surface topography and contact potential difference (CPD) between a given material and an AFM tip. KPFM can work at ambient conditions and distinguish variations in work function as small as 5 meV with spatial resolution down to several nanometers [21,22]. However, an absolute value of the work function reported by the KPFM depends greatly on the AFM tip conditions as well as the choice of reference materials, which

* Corresponding author.
E-mail address: rszoszkiewicz@chem.uw.edu.pl (R. Szoszkiewicz).

https://doi.org/10.1016/j.apsusc.2024.160578
Received 15 April 2024; Received in revised form 5 June 2024; Accepted 20 June 2024
Available online 21 June 2024
0169-4332/© 2024 The Author(s). Published by Elsevier B.V. This is an open access article under the CC BY-NC license (http://creativecommons.org/licenses/by-nc/4.0/).

are not necessary for PES.

In the case of MoS_2, experiments have showed that its measured work function on various substrates increases with thickness [23,24]. This phenomenon has been explained by interlayer screening effects of an electric field present at the MoS_2/substrate interface due to interfacial charges and dipoles. While influence of the interfacial electric field on WF should be eliminated at thickness larger than a screening length, there is a considerable discrepancy in reported WF values for thick MoS_2 flakes, which range from 4.8 to 5.7 eV [23–28]. Therefore, an appropriate value of the work function for thick MoS_2 samples is still elusive. Particularly that there are at least several contributing factors such as water and oxygen adsorbates [26,29,30] as well as fabrication methods and reference materials used for KPFM measurements.

In the case of MoO_3, ultraviolet photoelectron spectroscopy (UPS) studies have showed that MoO_3 monolayer on graphene has work function between 6.3–6.7 eV in vacuum, which decreases down to 4.7 eV for the samples exposed to ambient conditions [31]. Similarly, KPFM studies in air have showed that thin (2–7 layers) MoO_3 flakes on graphite display work function of 4.73 eV [32]. Furthermore, UPS measured work function of bulk MoO_3 to be 6.8 eV in vacuum and between 5.32 and 5.7 eV for samples exposed to air [33,34]. Finally, recent studies by UPS showed that thin films of MoO_x and MoO_xS_y on liquid metal droplets have work function of 5.1–5.2 eV [35,36]. For MoO_3/MoS_2 heterostructures, few studies have showed that oxidation of MoS_2 or deposition of MoO_3 on MoS_2 increases their work function [9,37,38]. However, to the best of our knowledge, there is no systematic study on the thickness dependence of MoO_3 work function in air for any of its typical substrates and heterostructures.

In this study, the work function has been investigated by the KPFM method in air. First, thick MoS_2 flakes fabricated by mechanical exfoliation have been tackled over many measurements to find their work function and investigate the effect of their surface contaminants. Next, various MoO_3 flakes with different thickness were thermally synthesized to study their work function. Later, thin oxide layers produced by heating the MoS_2 flakes at elevated temperature and relative humidity have been investigated. We observed that work function of as-exfoliated MoS_2 differed from the pristine MoS_2 due to exfoliation tape residues. In addition, MoO_3 on SiO_2 as well as MoO_3 on MoS_2 have showed thickness-dependent work function. We explained the results via invoking an electric field present at the MoO_3/substrate interface. Finally, we built an electrical junction based on an amorphous 1L MoO_3/MoS_2 heterostructure and studied its rectifying behavior.

2. Materials and methods

Freshly exfoliated MoS_2 flakes were obtained from laboratory grade 2H molybdenite crystals bought from SPI Supplies, West Chester, PA, USA, catalogue number #429MM-AB. The MoS_2 samples have been mechanically exfoliated using a standard blue tape and transferred on fine polished ⟨1 1 1⟩ Si crystals with resistivity more than 10,000 Ω.cm, bought from ITME, Warsaw, Poland. Prior to a sample transfer, the substrates were ultrasonically cleaned in sequential steps with deionized water, acetone, ethanol, and isopropanol for 10 min each. After each ultrasonication step, the substrate was dried with pure argon. At the end of ultrasonic cleaning, oxygen plasma (PE-25, Plasma Etch, 150 mTorr O_2, 100 W RF power, 180 s) was used to get rid of any remained residues/pollutants.

Heated and rastered MoS_2 flakes were prepared by heating freshly exfoliated MoS_2 flakes in air at 350–370 °C for 10–15 min on a standard hot plate. The samples were covered with a quartz Petri dish to insure a controlled atmosphere and proper distribution of temperatures within a heating zone. The hot plate was calibrated with a standard thermocouple and a Pt thermometer to yield a temperature error of ± 2 °C on the sample surface. In order to remove oxide residues (clusters) and expose clean MoS_2 surface, the heated flakes were further rastered by Cypher S AFM (Asylum Research, Goleta, CA, USA) in a contact mode in air with a MLCT-F cantilever (Bruker, Santa Barbara, CA, USA). An area on heated/oxidized MoS_2 surface were scratched several times at loads between 0.6 ± 0.1 and 12 ± 1 nN with a scanning rate between 2.60 and 4.88 Hz. Loads were calibrated from a spring constant and sensitivity factors, which were obtained from thermal resonance of the used cantilever using routines available within the data acquisition software.

Crystalline MoO_3: α-MoO_3 rods synthesized by chemical vapor transport (CVT) method were bought from HQ Graphene, Netherlands. α-MoO_3 flakes were synthesized by a modified hot plate method [39]. A molybdenum foil (99.9 %, 1 mm thickness, Sigma-Aldrich) were placed on a hot plate, and a grade V1 Muscovite mica disc (Agar Scientific) were placed on top of the Mo foil while heated at 540 °C for 40 min in air. For transferring the MoO_3 flakes from mica substrate to 300 nm-SiO_2/Si wafer, the Mica surface was covered by a viscoelastic polydimethylsiloxane (PDMS) film (Gelfilm from Gelpak) in contact with MoO_3 flakes. The edges of the PDMS film were gently peeled off, and the whole stack was ultrasonicated in a deionized water to let the water penetrate between the PDMS film and mica substrate. Due to high hydrophilic nature of mica, the water penetrated between mica and MoO_3 flakes resulting in separation of PDMS/MoO_3 from mica substrate. Then, the PDMS with MoO_3 flakes were dried with argon. Later, the flakes were transferred to a SiO_2/Si substrate by mechanical cleavage. Before transferring, the SiO_2/Si wafers were cleaned with the same procedure used for all substrates.

MoO_3/MoS_2 heterostructures were synthesized by heating freshly exfoliated MoS_2 flakes in a custom built chemical reactor [7,40] with an ability to maintain same pressure and relative humidity everywhere on the sample. Various temperatures (between 190 to 310 °C, with a maximum ± 15 °C error) and relative humidities (usually between 80 to 95 %) were utilized to grow one or more oxide layers on the MoS_2 surface. The reaction time was always around 10 min. After heating, an area on each flake was rastered by an AFM device to expose underlying MoS_2 surface for KPFM measurements and comparisons with non-oxidized MoS_2.

KPFM-AFM measurements were performed by Cypher S AFM double-pass amplitude-modulated KPFM with Pt/Ir coated ASYELEC-01-R2 cantilevers (Asylum Research) with a nominal spring constant of 2.8 N/m and nominal resonance frequency of 75 kHz. Topography images were collected simultaneously with the same cantilever. During the KPFM measurements, a bias voltage was applied to the tip, while the sample was grounded. Raw, i.e., untreated KPFM tip-sample CPD data in volts ("Nap potential") were analyzed using Gwyddion software. The values of the work function (WF) in electron-volts were obtained from the CPD values according to Eq. (1):

$$WF_{anyplace} = WF_{ref} + e(CPD_{anyplace} - CPD_{ref}) \quad (1)$$

where $e = 1$ and is an absolute value of the charge for one electron; CPD_{ref}, in volts, is the contact potential difference measured on the reference surface; $CPD_{any\ place}$, in volts, is the contact potential difference measured at the place of interest. An HOPG reference sample (Asylum Research, prod. no. 823.009) was chosen to calibrate the KPFM data and its WF of 4.6 eV was measured by UPS.

Conductive AFM measurements were performed utilizing Cypher S AFM with boron-doped diamond coated silicon AFM tips with spring constant of 2.8 ± 1.8 N/m under ambient conditions. After finding the regions of interest, small areas such as 8 × 8 nm were scanned in contact-mode with a small normal force in the range of few nN and a high scanning speed of more than 15 Hz. A bias voltage applied to the sample was tuned for each session independently.

UPS measurements on highly ordered pyrolytic graphite (HOPG) were performed by SPECS Surface Nano Analysis GmbH (Berlin, Germany) instrument with Microwave Ultraviolet Light Source (UVLS) using non-monochromatized He(II) and He(I) emission lines operating at He pressure of 2×10^{-3} mbar. Phoibos 150 hemispherical analyzer (150 mm radius) NAP version with 2D-DLD detector was used. The

system base pressure was in the 10^{-10} mbar range in detector chamber and 10^{-7} mbar range in sample chamber. UPS data were analyzed using CasaXPS version 2.3.24PR1.0 [41].

X-ray photoelectron spectroscopy (XPS) data was recorded on Kratos Axis Supra spectrometer, equipped with a monochromatic Al Kα radiation source (1486.7 eV) operating at 225 W. All data were collected with an analyzer pass energy of 80 eV for survey scan and 20 eV for region spectra respectively. The instrument work function was calibrated to give a BE of 84.0 ± 0.1 eV for the $4f_{7/2}$ line of metallic gold and the spectrometer dispersion was adjusted to give a BE of 932.6 eV for the Cu $2p_{3/2}$ line of metallic copper. The effect of sample charging was reduced by a neutralization system.

Raman studies were performed using a Horiba Jobin Yvon LabRAM HR800 Raman spectrometer with a 532.0 nm laser excitation line with 100 × objective lens and 1800 g mm^{-1} grating. The laser power was below 3 mV, and the spot size was ~4 μm.

SEM imaging was performed with a scanning electron–ion microscope Crossbeam 540× (Zeiss). The samples were imaged using an SESI and In-lens detectors (mix signal) at an accelerating voltage of 5 kV, a working distance from the column WD = 5 mm and a stage tilt of 0°.

Device fabrication: An MoS_2 flake was mechanically exfoliated by a standard blue tape from laboratory grade 2H molybdenite crystals on a 300 nm-SiO_2/undoped-Si substrate. The sample was heated in the same custom built chemical reactor in an humid environment as used for synthesis of MoO_3/MoS_2 heterostructures. A part of the flake was rastered by AFM in a contact mode to expose underlying MoS_2 surface. The electrode patterns on the flake were defined by a maskless photolithography method. Later, 15 nm Cr and 85 Au were deposited on the sample via sputtering to form Cr/Au contacts. The process was completed by a standard lift-off step to make a resulting device.

Density functional theory (DFT) calculations: Spin polarized DFT calculations were done with the code VASP [42,43]. The interaction between cores and electrons was treated with the Projector Augmented Wave approach [44,45]. O (2s, 2p), S (3s, 3p) and Mo (4d, 5s) electrons were treated explicitly. The Perdew, Burke and Ernzerhof (PBE) exchange and correlation potential was adopted [46]. The long-range dispersion forces were treated with the damped DFT-D3 method [47,48]. The plane-waves basis set was truncated with a 550 eV kinetic energy cutoff. A tolerance of 10^{-5} eV was adopted to truncate the electronic loop, while residual forces smaller than 10^{-2} eV/Å were required in the relaxation of the ionic positions. The sampling of the reciprocal space was reduced to the Γ point due to the large dimensions of the supercells. The charge transfer at the interface was evaluated recurring to the Bader formalism [49,50]. The Bader charges of all atoms belonging to each moiety of the heterojunction were summed up to obtain the total interfacial charge transfer. Spurious physical effects due to interfacial dipole moments were prevented by applying a counter dipole in the empty space above the slab [51]. The interface between MoS_2 and MoO_3 was built by deposing a monolayer of α-MoO_3 on three layers of MoS_2. A $(5 \times 2\sqrt{3})$ MoS_2 supercell was built underneath (4 × 3) supercell of MoO_3 (0 1 0). To minimize the strain related to the lattice mismatch, the lattice parameters of α-MoO_3 were then adapted to those of MoS_2, with small in-plane residual strains of 0.2 % × 1.3 %. An empty space of at least 20 Å was added in the supercell. With an analogous approach, the interface between MoO_3 and silica quartz was built from (2 × 2)MoO_3 R90°/(3 × 3)SiO_2 coincidence lattice, with later obtained residual strains of 3.8 % × 0.3 % released on MoO_3.

3. Results and discussion

3.1. Careful investigations of the MoS_2 samples

Work function of various freshly exfoliated MoS_2 samples on silicon substrates were studied by KPFM measurements. Only the MoS_2 flakes with thickness of more than 25 nm, i.e., more than the screening length of MoS_2 on silicon-based substrates were chosen. This was to remove effects of the electric field at the MoS_2/substrate interface on the work function. In addition, care was taken to avoid budged out flakes. An HOPG sample served as a reference due to its stability in ambient conditions and lack of surface dipoles [37,52]. UPS measurements were performed on HOPG to obtain its work function. During each KPFM session, the contact potential difference (CPD) values were measured.

Fig. 1a presents a typical UPS spectrum on HOPG, which shows the work function of 4.60 eV. To carefully investigate each MoS_2 sample, first CPD values were obtained on HOPG, then on a given flake, and finally once again on HOPG. This is because the CPD signal is highly dependent on the AFM tip conditions which may change during scanning as showed in SEM images of fresh and used tips in Figure S1.

Fig. 1b,c show the CPD images of two freshly exfoliated MoS_2 flakes, called later "as exfoliated" samples, measured in one session. Their mean CPD values were 687 ± 62 and 750 ± 45 mV, respectively. The CPD values on HOPG measured prior to these samples was 333 ± 4 mV, and after these MoS_2 samples was 431 ± 20 mV. Next, the CPD differences, ΔCPD, between each pair of the corresponding HOPG and MoS_2 measurements were considered for the calculations of the MoS_2 work function. Herein, we obtained ΔCPD of 354 ± 66 and 256 ± 82 mV for the first MoS_2 sample and 417 ± 49 and 319 ± 65 mV for the second MoS_2 sample. Table S1 shows all ΔCPD values obtained for eight freshly exfoliated MoS_2 flakes from 29 measurements including HOPG. For each flake, mean ΔCPD was used to obtain mean work function through Eq. (1). By considering the HOPG WF to be 4.60 eV, the obtained WF values for the flakes in Fig. 1b,c were 4.91 ± 0.06 and 4.97 ± 0.09 eV, respectively. Another example of such measurements is reported in Figure S2. Overall, the work function obtained for "as exfoliated" MoS_2 flakes was in the range of 4.85 to 5.06 eV with a mean value of 4.93 ± 0.16 eV. The error is a studentized standard deviation at 95 % confidence level.

Mechanically exfoliated MoS_2 samples, although easy to prepare, are usually contaminated by exfoliation tape residues, which do not necessarily stick to an AFM tip, but can affect the values of the obtained work function. In order to eliminate such contributions, the work function value for a pristine 2H MoS_2 sample was obtained. For this reason, several mechanically exfoliated MoS_2 samples were heated at 370 °C for 15 min to evaporate tape residues similarly as in Refs [6,53]. However, at such conditions, oxidative etching of the MoS_2 flakes occurred as well. Therein, most of the etched products leave the surface and expose fresh underlying MoS_2 basal planes. Nevertheless, some MoO_x species remain in the form of small clusters and increase slightly the measured WF of the MoS_2 surface [7,54]. Thus, prior to KPFM measurements, the heated samples were rastered by an AFM tip several times to sweep out the MoO_x residues and expose intact MoS_2 surface [54].

Fig. 1d shows the CPD value over the scanned area on a "pristine" MoS_2 sample. The obtained work function with reference to HOPG was 4.83 ± 0.01 eV. The results of same experiments, but performed on two other sets of MoS_2 and HOPG samples are presented in Figure S3 and Table S2. Overall, the work function for "pristine" MoS_2 flakes were between 4.83 to 4.87 eV with a mean value of 4.85 ± 0.09 eV. The error is a studentized standard deviation at 95 % confidence level.

To conclude, we observed larger WF values and their larger errors for the "as exfoliated" samples in comparison to their "pristine" counterparts. These differences can originate from tape residues, air-borne adsorbates and presence of Mo oxides. Both kinds of samples were exposed to the same environment for very similar periods of time. Thus, air-born adsorbates do not contribute to the differences between their work functions. Moreover, based on a detailed discussion of Figure S4 presented in the Supplementary data, we exclude the effects originating from Mo oxides. Consequently, we attribute the observed higher WF values in the case of "as exfoliated" samples to exfoliation tape remainders present on their surface in comparison to the "pristine" samples.

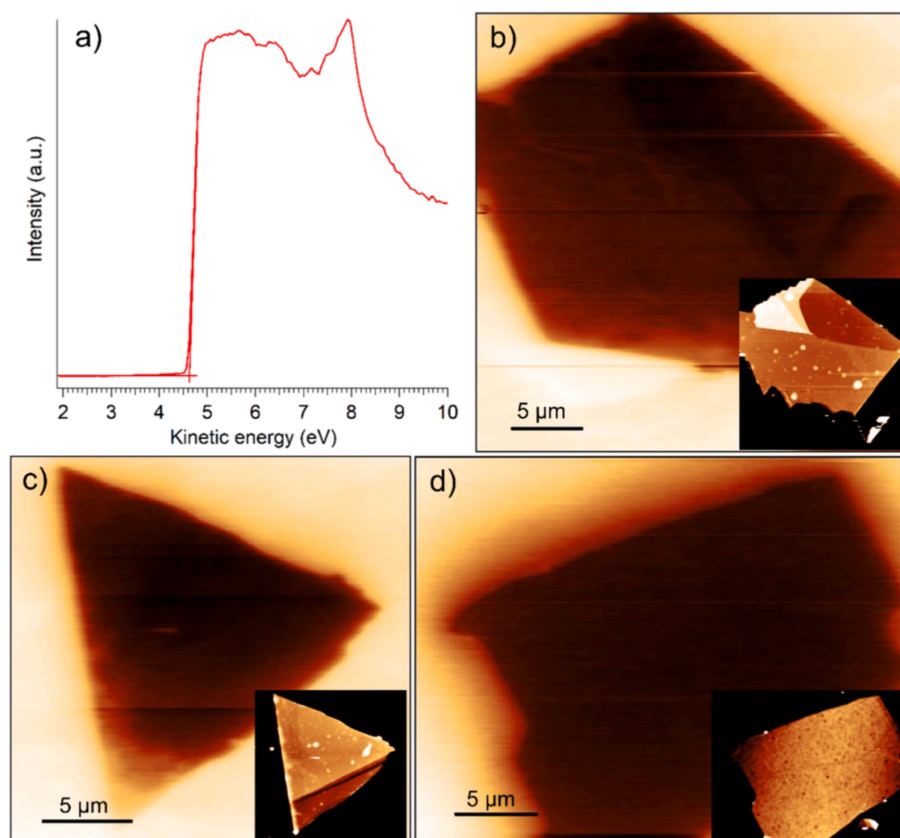

Fig. 1. (a) UPS studies on HOPG and (b-d) KPFM measurements on MoS_2 samples. (b, c) CPD images of two different "as exfoliated" MoS_2 flakes with calculated WF of 4.91 ± 0.06 and 4.97 ± 0.09 eV, respectively. (d) CPD image of a "pristine" MoS_2 flake (with some etch pits) with calculated WF of 4.83 ± 0.01. The Z-scales in (b-d) are 462, 577, and 390 mV, respectively. Brighter colors represent higher CPD or height values. Insets show corresponding topography images.

3.2. *Careful investigations of MoO_3 samples*

Next, we embark on finding the WF values on various MoO_3 samples. To start with, bulk MoO_3 samples were considered in a form of thick MoO_3 rods synthesized by a CVT method. Examples of typical Raman spectra as well as KPFM measurement of such rods obtained by using HOPG as the reference sample are presented in Figure S5. The three rods studied by KPFM method showed mean WF of 5.46 ± 0.1 eV. This value is close to the UPS-reported WF of 5.42 eV for air-exposed molybdenum oxide films [55] and 5.49 eV for evaporated MoO_3 films [56]. Our measurements verify that very thick MoO_3 samples in air show substantially lower work function than in vacuum (6.8 eV).

Later, the effect of MoO_3 thickness on the work function for crystalline MoO_3 in air was studied. For this purpose, various MoO_3 flakes were synthesized directly on mica by the modified hot-plate method and transferred onto 300 nm thick SiO_2 atop Si substrates. Previous analyses have showed that such approach produces crystalline MoO_3 [39]. Same conclusion is reached from Raman spectra collected on our samples. Fig. 2a shows Raman spectra of the mica substrate as well as MoO_3 flakes before and after transfer. The mica substrate shows sharp peaks at around 258 and 816 cm^{-1} as well as broad peaks at 213, 407, 630, 747, 907 cm^{-1}. MoO_3 flakes on both substrates show clearly the characteristic bands of crystalline MoO_3 at 664–670 (B_{3g} νOMo_3), 817 (B_{1g} νOMo_2), and 994 (B_{1g} νO = Mo) cm^{-1}, as well as less known Raman bands at 283 (B_{2g} δO = Mo), 332–336 (A_g δOMo_3), and 363 (A_g δO = Mo) [57,58].

The work function of the MoO_3 flakes with various thickness was measured with respect to SiO_2 substrates. The SiO_2 WF value was obtained by KPFM measurements with respect to HOPG, which are presented in Figure S6 and yield WF of 5.05 ± 0.02 eV. This value was additionally cross-checked with a MoS_2 flake as a reference (see Figure S7) and agrees with a literature value of 5.05 eV [26].

Fig. 2b shows a topography profile of a monolayer (1L) MoO_3 with thickness of 0.7 nm transferred onto SiO_2 substrate. Corresponding CPD profile in Fig. 2c shows that such a layer had 21 ± 6 mV lower CPD respect to the substrate yielding the WF of 1L MoO_3 to be 5.03 ± 0.01 eV. Similarly, 3L and 9L MoO_3 showed in Fig. 2d,e produced −12 ± 6 and 10 ± 7 mV CPD difference with respect to the substrate, resulting in WF of 5.04 ± 0.01 and 5.06 ± 0.01 eV, respectively. The same procedure was repeated for several thicker MoO_3 flakes transferred onto SiO_2. For example, the MoO_3 flakes with thickness of 190 and 450 layers in Fig. 2f,g showed work function of 5.39 ± 0.01 and 5.46 ± 0.01 eV. Fig. 2h plots the work function of all the investigated MoO_3 flakes with various thickness vs. their number of layers. The WF increases with the number of layers levelling off at 5.46 eV. The result matches very well with our aforementioned studies of thick MoO_3 crystals and confirms that 5.46 eV is indeed the bulk WF value for crystalline MoO_3 in air.

Various KPFM studies have already showed that layered materials such as MoS_2 on variety of substrates (including SiO_2) display a thickness-dependent work function [23,24,26]. It has been attributed to screening of the electric field present at the material/substrate interface. In the case of SiO_2 substrates such electric field originated from charged impurities such as trapped charges or surface adsorbates [23,59,60]. To describe the screening effects, the following model [23,59,61] has been used. First, the screening constant (K), related to the Thomas-Fermi screening length, has been defined as a ratio of the screened potential from the interfacial charges felt within a given layer, $V_{sc}[L]$, to its value at a previous layer, $V_{sc}[L-1]$:

$$V_{sc}[L] = KV_{sc}[L-1] \text{ (applies for } L > 1) \quad (2)$$

Eq. (2) holds true when an electrostatic potential produced by interfacial charges is constant with respect to vertical distance. This

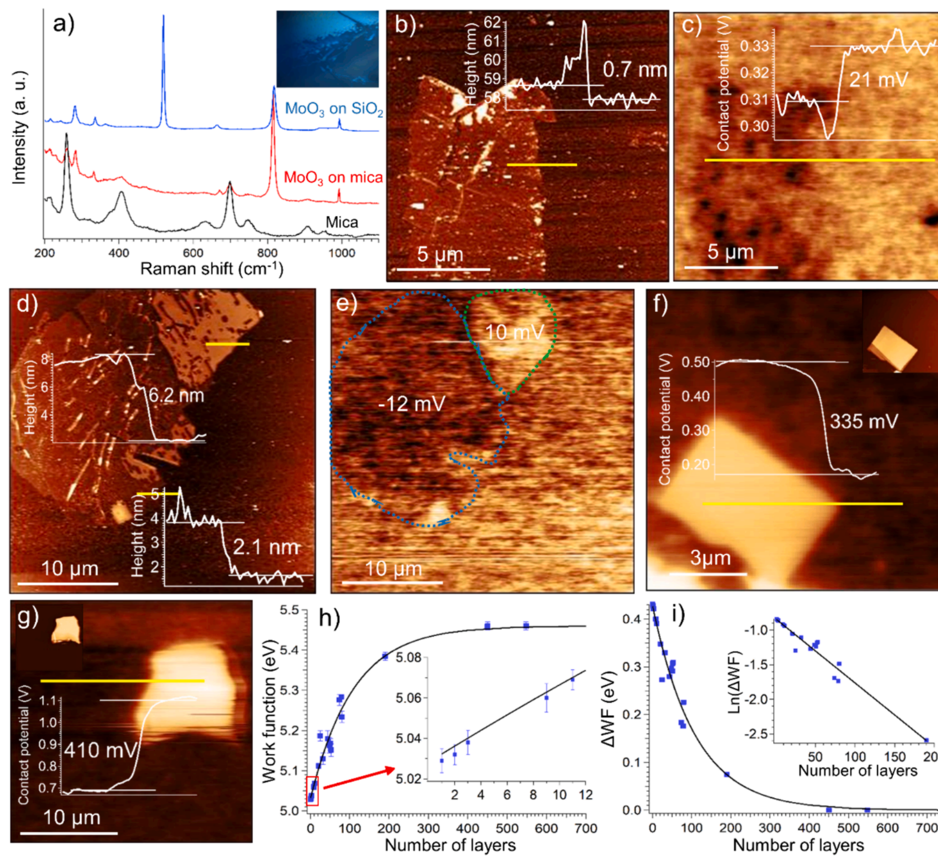

Fig. 2. KPFM studies on MoO_3 flakes: (a) Raman spectra of MoO_3 flakes on mica and SiO_2/Si (with Si peak at 520 cm^{-1}) together with a spectrum of bare mica. Inset shows an optical image of the MoO_3 film synthesized on mica. (b) Topography and (c) CPD images of a MoO_3 monolayer transferred from mica to SiO_2/Si. Insets show representative height and contact potential profiles along the yellow lines. Z-scales in (b) and (c) are 11.6 nm and 90 mV, respectively. (d) Topography and (e) CPD images of MoO_3 flakes with 3 and 9 layers onto SiO_2. Insets in (d) show the topography profiles along the yellow lines. Dotted blue and green circles in (e) mark the 3- and 9-layered MoO_3 flakes, respectively. Z-scales in (d) and (e) are 15.6 nm and 46 mV, respectively. (f, g) CPD images of 190 and 450 MoO_3 layers on SiO_2, respectively. Insets show corresponding topography images and representative contact potential profiles along the yellow lines. Z-scales in (f) and (g) are 500 and 400 mV, respectively. Brighter colors represent higher CPD or height values. (h) Work function of MoO_3 flakes on SiO_2 substrate vs. number of layers. Inset shows a magnified view of data in a red box. (i) ΔWF of MoO_3 flakes vs. number of layers. Inset shows the natural logarithm of ΔWF vs. number of layers. (For interpretation of the references to colour in this figure legend, the reader is referred to the web version of this article.)

assumption is justified by an electrostatic model of a charged plate with lateral dimensions being much larger than vertical distances considered, see Supplementary data for more details and derivations.

By combining Eqs. (1) and (2), the work function $WF[L]$ measured at each MoO_3 layer is obtained as follows:

$$\begin{aligned} WF[L] &= e\left(V_{MoO_3}[L] - V_{SiO_2}\right) = e\left(V_{MoO_3} + V_{sc}[L] - V_{SiO_2}\right) \\ &= e\left(V_{MoO_3} - V_{SiO_2}\right) + eV_{sc}[L] = WF[bulk] + eK^{L-1}V_{sc}[1] \end{aligned} \quad (3)$$

In Eq. (3), $V_{MoO_3}[L]$ is the CPD measured at a layer L of the MoO_3 oxide, V_{MoO_3} is the CPD of the bulk MoO_3 and V_{SiO_2} is the CPD of the SiO_2 substrate.

By rearranging Eq. (3) to calculate $\Delta\ WF = WF[bulk] - WF[L]$ and taking its natural logarithm, we obtain the values of K and V_{sc} $[L = 1]$ from the experimental data. Fig. 2i shows ΔWF values plotted against the number of MoO_3 layers on SiO_2 with $WF[bulk] = 5.46$ eV. We obtain a very good fit with $K = 0.991 \pm 0.001$ and $V_{sc}[1] = -0.428 \pm 0.016$ V. Using the values of K and $V_{sc}[1]$ we also fit the data in Fig. 2h. Once again we obtain a very good agreement, which shows that the approach taken was satisfactory to model the WF dependence for MoO_3 flakes with various thickness on SiO_2.

Consequently, we conclude that the effect of MoO_3 thickness on its WF originates from screening of interfacial charges. Our results can also explain some earlier studies in air. For example, in one of such studies, the work function of 17L MoO_3 on SiO_2 was reported to be 40 meV higher than that of 7L MoO_3 on SiO_2 [62]. Using our results, one obtains 36 meV for WF difference between such MoO_3 flakes.

As a corollary, the value of K (=0.99) is larger than that of MoS_2 on SiO_2 (0.94) [23], which can be explained via substantial difference in polarizability between MoO_3 and MoS_2. The relative dielectric constant of thin MoO_3 films, ε_{MoO3}, has been reported to be around 35 [63], while in the case of MoS_2 nanosheets the value of ε_{MoS2} is between 3 and 7 [64,65]. Much higher ε_{MoO3} than ε_{MoS2} means larger polarizability of the MoO_3 with respect to MoS_2 and consequently larger screening length and larger K value. Similar conclusions are obtained from a more detailed analysis using a screened Coulomb potential, see Supplementary data. Moreover, our absolute value of $V_{sc}[1]$ is larger than that obtained for MoS_2 in the literature (0.30 V) [23], which means more interfacial charges trapped at MoO_3/SiO_2 interface than at MoS_2/SiO_2 interface.

3.3. Careful investigations of amorphous MoO_3/MoS_2 heterostructures

In this part, the work function of the molybdenum oxide structures formed onto MoS_2 during its oxidation in humid environment has been investigated. To produce oxide/MoS_2 structures with various oxide thickness several MoS_2 flakes were heated at high temperature and humid environment within a closed chemical reactor. After oxidation, some parts of the flakes were rastered several times by an AFM tip in a contact mode to remove oxides and expose fresh MoS_2 surface for

further KPFM analyses. Fig. 3 shows topography and contact potential images of a typical sample. An unrastered area is about 0.7 nm higher than the rastered region, suggesting the formation of one MoO_3 layer atop MoS_2 during heating at high humidity. Magnified portion of the AFM topograph in Fig. 3b show a textured oxide surface with twice the roughness of the underlying MoS_2 surface. It appears to be composed of small oxide islands, which are interconnected and form a continuous layer. The CPD image in Fig. 3c shows that the oxide layer has 122 ± 10 mV higher work function than the MoS_2 surface.

Previous AES, XPS, and XAS spectroscopies have already showed that heating MoS_2 flakes at similar temperatures in dry and humid air results in formation of mostly MoO_3 structures in the forms of single clusters [54], islands and layers [7]. Moreover, presence of H_2O molecules has been showed to produce some surface oxides in laser heating of other transition metal dichalcogenides [66]. Herein, we elaborate on the chemistry of the Mo oxide layer via the structural studies using fast scanning conductive AFM (c-AFM) measurements. Recent studies have showed that such novel c-AFM measurements are able to resolve true atomic structures of various 2D materials including MoS_2 [67].

Fig. 4a shows a c-AFM current image of the MoS_2 surface. A perfect hexagonal arrangement of sulfur atoms is easily noticed together with one randomly present single sulfur vacancy. The interatomic spacing between sulfurs is 0.32 nm, which matches a literature value [67]. Besides sulfur vacancies, we also found a Moiré pattern, which is very surprising, but can been seen as an intrinsic defect in a mechanically exfoliated MoS_2 flake. Such Moiré patterns, here: a superlattice of two placed atop and mutually twisted MoS_2 layers, have been previously observed only in heterostructures twisted either purposefully or via stress-mediated synthesis [68–70]. Fig. 4b,c as well as Figure S10 show that a top-most MoS_2 layer is either naturally twisted with respect to its underlying layer or it is rather a remainder of a mechanically exfoliated layer, which stuck back to the flake. The resulting Moiré pattern in this case corresponds to a twisting angle of ca. 1.5°, which has been calculated from the dimensions of a superlattice produced with two superimposed sulfur layers, see Fig. 4c.

Fig. 5 shows a c-AFM current image of the thermally oxidized MoS_2 flakes in humid air. Unfortunately, due to high stiffness of the scanning probe and inability to apply and control extremely low forces during fast scanning, such c-AFM measurements tend to raster most of the scanned oxide layer. This process is visualized in Figures S11,12. While most of the oxides was removed during c-AFM imaging, some oxide nanocrystallites remained on the surface. As showed in Fig. 5b,c their atomic structure was different from MoS_2. Strikingly, out of several possible Mo oxide structures, their atomic arrangement matched configuration of top oxygen atoms within MoO_6 octahedral building blocks in either orthorhombic α-MoO_3 or monoclinic β-MoO_3 structures. From the two clusters exemplified in Fig. 5b,c we obtained the atomic distances $x_1 = 0.415 \pm 0.005$ and $x_2 = 0.365 \pm 0.005$ nm counted along yellow and green crossectional lines, respectively. In addition, we measured the angles between yellow and green lines to be 85 ± 2° and 95 ± 2°. The distances and angle reported for an α-MoO_3 crystal structure between top oxygen atoms are $a = 0.396$ nm, $c = 0.370$ nm and $\beta = 90°$. The corresponding distances along two perpendicular directions for the β-MoO_3 crystal structure are 0.400 nm and 0.372 nm. Orthorhombic and tetragonal MoO_2 do not match our results since mean distances between their top oxygen atoms are ca. 0.34 nm, which is substantially less than obtained here atomic distances, see Table S3 for a detailed crystallographic comparison between various Mo oxide structures. Furthermore, through S-TEM measurements on epitaxial MoO_3 onto MoS_2, Yoon et al. [71] found out that the angles between a and c distances were indeed 85 and 95°, like in Fig. 5. Thus, we conclude that the crystallites in Fig. 5 are indeed the molybdenum oxides in the form of either α-MoO_3 or β-MoO_3. Both structures are thermodynamically allowed at our experimental conditions [72].

Interestingly, all MoO_3 crystallites show the same orientation indicating their preferential growth direction with respect to an underlying MoS_2 surface. This has been already observed by other studies [71] and it suggests that despite a lattice mismatch between MoS_2 and MoO_3, the latter can indeed form a quite conformal crystalline layer atop MoS_2. However, a typical grain size for these crystallites is between 1 to 2 nm. In addition, based on our previous studies, the MoO_3 crystallites originated most likely from single MoO_3 monomers attached to MoS_2 substrate at the single sulfur vacancies [54], which grew and formed such crystallites by help of humidity and likely through readsorption and surface diffusion of additional oxide species [40]. Contrasting detected small MoO_3 crystallites with a textured Mo oxide surface in Fig. 3b, we conclude that the Mo oxide layer is a mixture of amorphous and nanocrystalline MoO_3 oxides. These conclusions are supported by the XPS data showed in Fig. 5d, which was obtained on bulk MoS_2 thermally treated at the same conditions. The binding energy in the XPS spectrum is calibrated by C 1 s peak positioned at 284 eV [73]. The peaks at 235.7 and 232.8 eV are attributed to binding energies of Mo^{6+} $3d_{3/2}$ and $3d_{5/2}$ orbitals in MoO_3. Peaks at 234.8 and 231.7 are attributed to Mo^{5+} $3d_{3/2}$ and $3d_{5/2}$ orbitals [73]. Peaks at 232.6, 229.5, and 226.6 are attributed to Mo^{4+} $3d_{3/2}$, Mo^{4+} $3d_{5/2}$, S^{2-} 2 s orbitals in MoS_2 [74]. During peak fitting asymmetric Lorentzian line shapes were used and the relative peak areas as well as full widths at half maximums were fixed to 2:3 and 1:1 ratios for each set of the respective Mo $3d_{3/2}$ and Mo $3d_{5/2}$ pairs. The best fit to the XPS spectrum was obtained when a small amount of Mo^{5+} was considered in addition to Mo^{4+} and Mo^{6+}. This indicates the

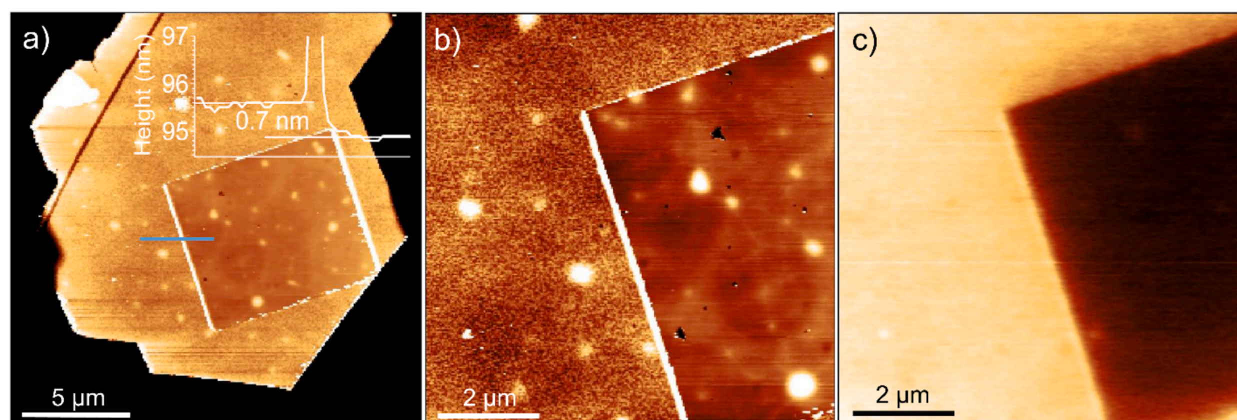

Fig. 3. (a, b) Topography and (c) CPD images of a MoS_2 flake oxidized at high humidity within a chemical reactor. A central square zone was rastered by an AFM tip in a contact mode to expose fresh MoS_2 substrate. Insets in (a) shows the height profile along a blue line stretching from oxidized to rastered areas. Thickness of an oxide layer is 0.7 nm. Z-scale in (a-c) are 5.9 nm, 2.27 nm, and 0.17 V respectively. Brighter colors represent higher CPD or height values. (For interpretation of the references to colour in this figure legend, the reader is referred to the web version of this article.)

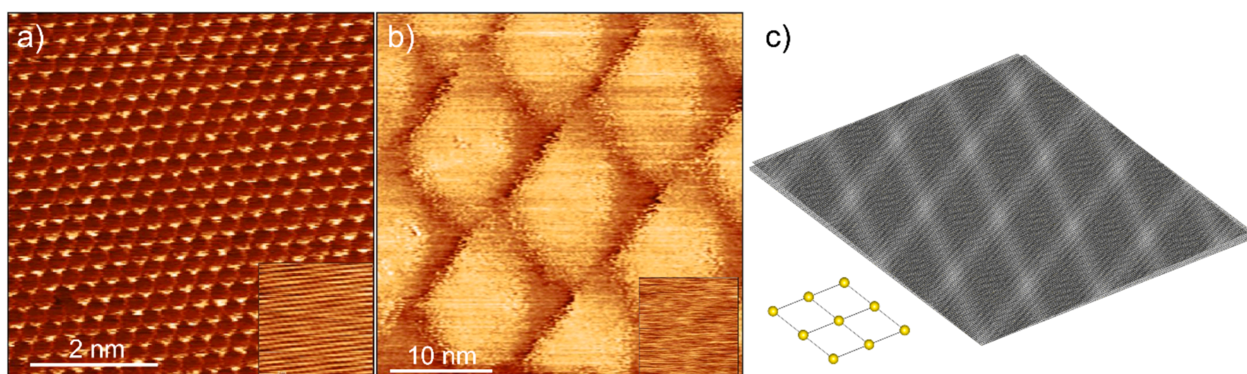

Fig. 4. Atomic resolution c-AFM studies on MoS_2 surface in air. (a) c-AFM current image of a thick MoS_2 surface showing hexagonal structure of top-most sulfur atoms with one visible single sulfur vacancy. Inset in (a) shows a corresponding and blurry AFM topography image, which does not resolve any atomic structure. (b) Rarely spotted c-AFM current image of a thick MoS_2 surface showing the Moiré pattern. Inset in (b) shows a respective topography image, which does not show any thickness change. Z-scales in (a) and (b) are 15 and 0.55nA, respectively. (c) a model of two superimposed hexagonal arrangements of sulfur layers twisted with respect to each other by 1.5°. Inset shows a top-view of sulfur arrangement in an underlying MoS_2 surface (not to scale with the pattern).

Fig. 5. (a-c) High resolution c-AFM studies on oxidized MoS_2 flakes and (d) XPS spectrum on oxidized bulk MoS_2. Current maps of a single oxidized flake at various magnifications, showing oxide crystallites matching the α or β-MoO_3 structure, with lattice parameters obtained from the crossectional yellow (x_1) and green (x_2) lines in (b) and (c). Inset in (a) shows a corresponding topography image, which could not resolve atomic structure. Insets in (b) and (c) show distance profiles along crossectional lines. Z-scale is 140 pA in (a) and 230 pA in (b) and (c). The digital lateral resolution is 0.63 Å in (b) and (c). (For interpretation of the references to colour in this figure legend, the reader is referred to the web version of this article.)

presence of oxygen vacancies in MoO_3 and its amorphous nature [73]. In addition, small amount of surface-adsorbed species such as hydroxylated oxygens [73] was detected in the O 1s XPS spectrum, see Figure S13 in Supplementary data.

To investigate relationships between WF and thickness of the Mo oxide layer onto MoS_2 flakes, various MoO_3/MoS_2 heterostructures were produced within the chemical reactor. Oxide layers with thickness of more than 4.2 nm were not detected, which confirms that thermal oxidation of MoS_2 crystal is a self-limiting process. Fig. 6 presents the KPFM measurements for the investigated samples. To obtain their work

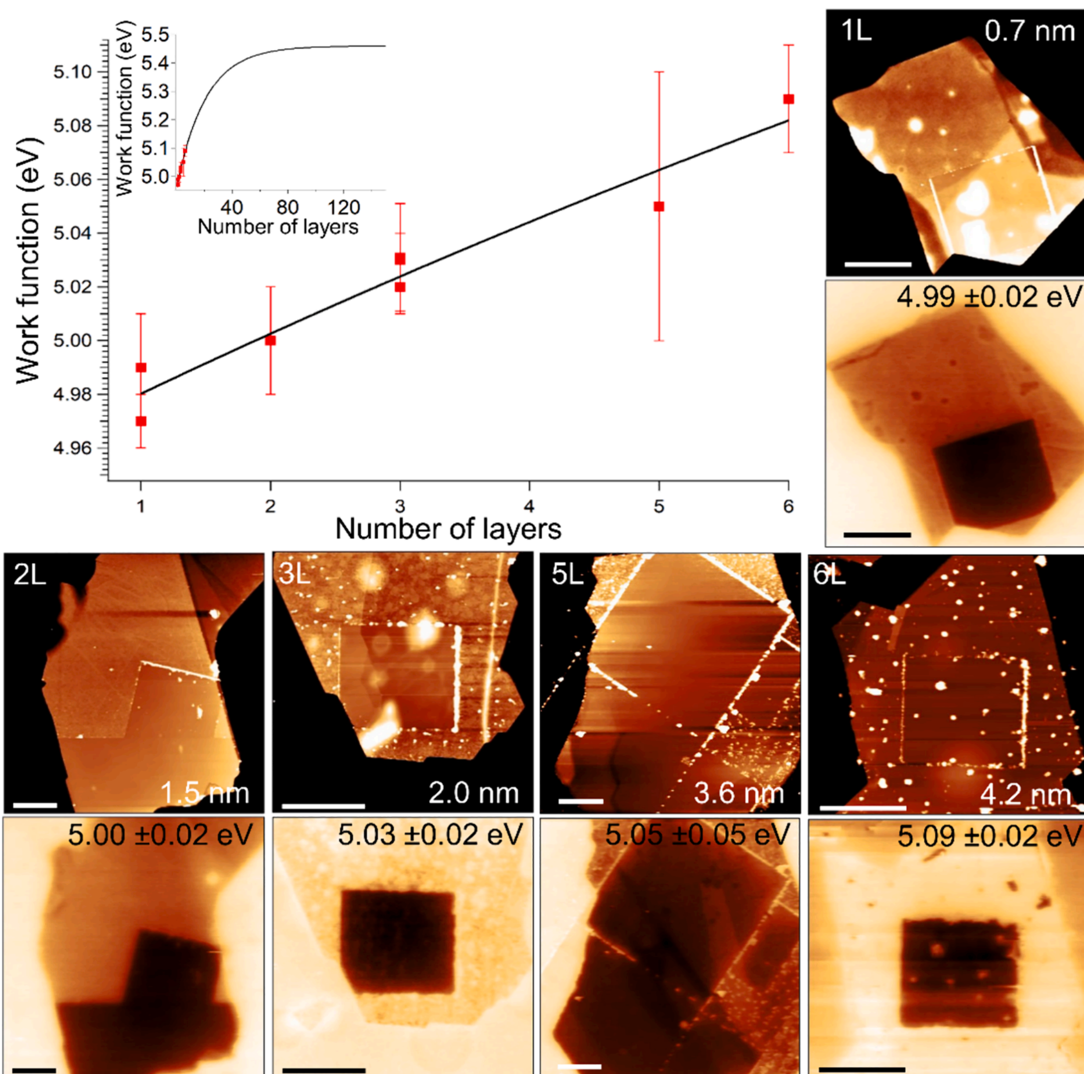

Fig. 6. A plot of the work function for MoO_3/MoS_2 heterostructures with various oxide thickness along with topography and CPD images for the samples denoted from "1L" to "6L". A portion of each sample has been rastered to measure the CPD of an underlying MoS_2 substrate. For each pair, topography is placed above CPD. Scale bars are 5 μm.

function, the WF of a MoS_2 substrate was considered to be 4.85 eV as obtained earlier for the "pristine" MoS_2 flakes. Similarly to MoO_3 on SiO_2 presented in Fig. 2, the WF grows with thickness of the oxide layer. To explain this dependence, we use the screening charges model presented in Eq. (3) and consider the bulk MoO_3 work function of 5.46 eV, which we obtained earlier. Fitting the model to the data in Fig. 6, we obtain an excellent agreement with the values of K and $V_{sc}[1]$ being 0.953 ± 0.005 and -0.480 ± 0.005 V, respectively. The fit results match also other, previously published experimental data. For example, Zhang et al. [9] observed 260 meV difference in work function between their amorphous 6 nm MoO_3 film and an underlying MoS_2 flake. Using our fit, one obtains 267 meV in their case.

In order to investigate the electrical properties of the MoO_3/MoS_2 heterostructures, electrical connections were fabricated on a heterostructure placed onto undoped Si covered with 300 nm SiO_2 by depositing Cr/Au electrodes on its MoS_2 and oxide regions. Fig. 7a shows a topography profile of this heterostructure with one MoO_3 layer. Next, the I-V measurements were performed on this device in ambient conditions and between various electrodes, as presented in Fig. 7b. The I-V curves show non-ohmic behavior, and in the case of the MoS_2 alone – electrodes 1 and 2 – we obtain very similar current values as in another work for the same voltage window [75]. The MoS_2 I-V curve can be understood as originating from two reversely biased metal/MoS_2 Schottky contacts in series. Similarly, oxidized MoS_2 alone (electrodes 3 and 4) can be understood as two reversely biased metal/oxidized MoS_2 Schottky contacts in series. Furthermore, our complementary c-AFM I-V studies, see Supplementary data and Figure S14 therein, show that the Schottky barrier is larger in the case of metal/oxidized MoS_2 than in the case of metal/MoS_2. However, instead of symmetric I-V behavior expected in both cases, we observe asymmetry, which we attribute to geometrical reasons such as different contact areas between each electrode within respective pairs.

Symmetric I-V curves would yield rectification ratios (RRs) of one. Observed here small asymmetry yields still small RRs of 5.0 ± 0.5 and 4.1 ± 0.6 calculated between 2 to 4 V of source voltage for MoS_2 and oxidized MoS_2, respectively. However, the RR of 28 ± 7 in the same voltage range is obtained from the I-V curve on the MoO_3/MoS_2 heterostructure. Much larger RR for the heterostructure than in the cases of MoS_2 (or MoO_3) alone confirms the diode-like character of the MoS_2/oxidized MoS_2 junction. In addition, one also observes a smaller reverse leakage current in the heterostructure than in the case of MoS_2 (or MoO_3) alone. All this points out towards the p-n diode character of the heterostructure comparing to the Schottky character of the MoS_2 (or MoO_3) contacts alone. This, in turn, is likely a consequence of a

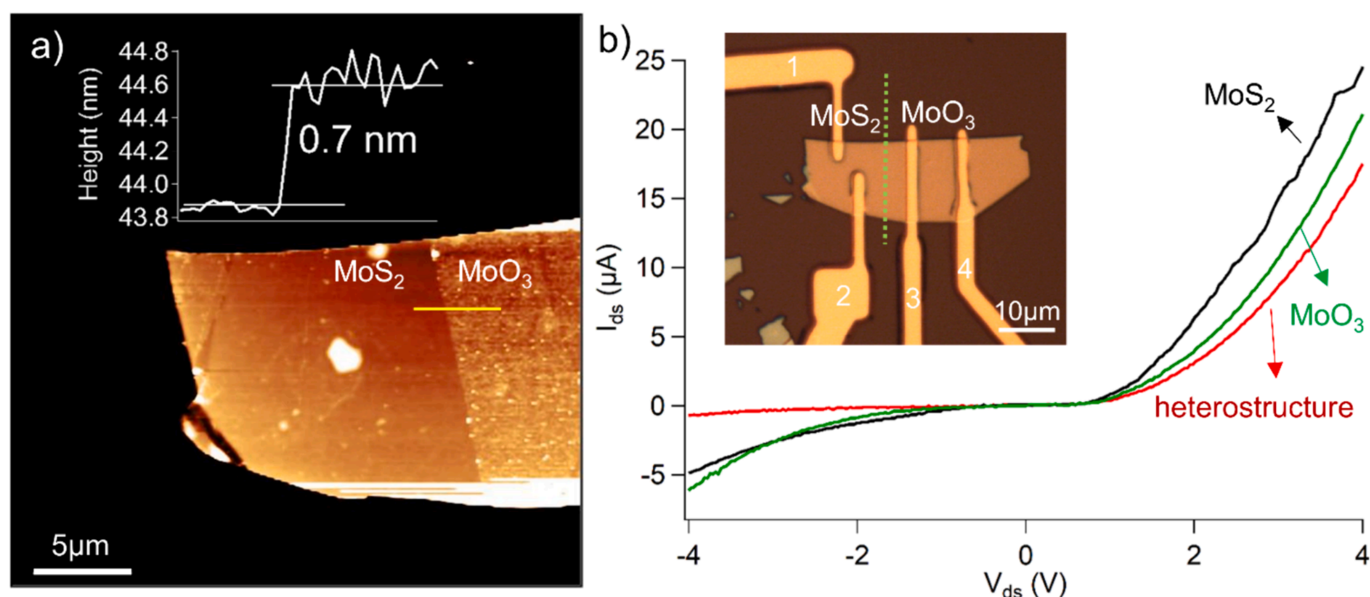

Fig. 7. Fabricated p-n junction based on a MoO_3/MoS_2 heterostructure. (a) Topography image of the heterostructure. Inset shows the topography profile along a yellow line. Z-scale is 8.3 nm and brighter colors represent higher heights. (b) Plots of drain-to-source current (I_{ds}) versus drain-to-source voltage (V_{ds}) at zero gate voltage between various electrodes: heterostructure (electrodes 1 and 3), MoS_2 (electrodes 1 and 2) and MoO_3 (electrodes 3 and 4). Inset shows an optical image of the device. Dashed green line in the inset separates MoS_2 from MoO_3. (For interpretation of the references to colour in this figure legend, the reader is referred to the web version of this article.)

substantial electron transfer from the MoS_2 to the oxide layer, which induces its substantial p-doping and is confirmed by our DFT calculations, see later.

3.4. Comparisons among various WF results

Table 1 combines work function values obtained for all the investigated here MoS_2 and MoO_3 samples as well as their heterostructures. To start with, the mean WF value on freshly exfoliated MoS_2 samples is slightly higher than the WF of “pristine” MoS_2 structures, which we attributed to tape residues. However, the discrepancy between these values is only a few percent, and minimum WF on “as exfoliated” samples matches the “mean” WF value for “pristine” samples. Therefore, typical measurements in air for freshly prepared MoS_2 samples are expected to overestimate the true MoS_2 work function only slightly.

For all bulk, i.e., μm and sub-μm thick MoO_3 samples in air we obtained WF of 5.46 eV. However, for thin MoO_3 layers investigated on two substrates, SiO_2 and MoS_2, we observed a thickness-dependent work function. This was explained to a satisfactory level by including only electrostatic contributions from interfacial electric fields and without invoking any additional thickness-dependent potentials.

Negative value of the $V_{sc}[1]$ and consequently lower work function of thin MoO_3 layers in comparison to their bulk values show that first MoO_3 layer is negatively charged on both MoS_2 and SiO_2 substrates. We estimated a surface charge density in the case of MoO_3/MoS_2 through simple electrostatic formulas applied to the KPFM studies, see Supplementary data, and the resulted value matched the density of trapped charges in MoS_2-based transistors [2,76,77]. An electron transfer mechanism from MoS_2 to MoO_3 has been also showed by DFT calculations [78]. In the case of MoO_3 on SiO_2 negative surface potential resembles the effects of the interfacial trap states provoked by charged impurities in silica at the MoS_2/SiO_2 interface [59,79].

Table 1
Comparison of the WF values obtained for the investigated structures.

Structure	Mean WF (eV)	Minimum WF (eV)	Maximum WF (eV)
As-exfoliated thick MoS_2	4.93 ± 0.16	4.85 ± 0.04	4.97 ± 0.09
“Pristine” thick MoS_2	4.85 ± 0.09	–	–
Thick CVT-synthesized MoO_3	5.46 ± 0.02 eV	–	–
MoO_3 flake on SiO_2 $K = 0.991$ $V_{sc}[1] = -0.428$ V	–	5.03 ± 0.01 (1L thick)	5.46 ± 0.01 (450L and 548L thick)
MoO_3/MoS_2 heterostructure $K = 0.953$ $V_{sc}[1] = -0.480$ V	–	4.97 ± 0.01 (1L MoO_3)	5.09 ± 0.02 (6L MoO_3)

To explore further the electron transfer mechanism, we provide a uniform DFT picture at the MoO_3/MoS_2 interface and at the MoO_3/SiO_2 interface (which, at the best of our knowledge, has not been studied before). The DFT calculations on α-MoO_3 monolayers were performed on the following three substrates: MoS_2 as well as fully hydroxylated quartz (1 0 0) SiO_2 slabs without and with charge-donor impurities trapped at the interface between silica and MoO_3 monolayer. In the case of MoS_2 substrate, we obtain that MoO_3 monolayer is negatively charged by -5.10×10^{13} $|e|$ cm^{-2}, corresponding to -0.88 $|e|$/supercell. The projected density of states (PDOS) plot in Fig. 8a shows the significant upshifting of the Fermi level in the heterojunction after contact with respect to the Fermi level of pristine, free-standing MoO_3, indicating n-type doping of MoO_3 by MoS_2. On a model displaying a sharp interface between MoO_3 and SiO_2, without any impurity or charge-trapping defect, the charge injected from the silica substrate into the MoO_3 monolayer is -2.73×10^{12} $|e|$ cm^{-2}. This corresponds to only -0.07 $|e|$/supercell, a value compatible with phenomena of reciprocal mixing and polarization of the orbitals at the interface. The PDOS plot shown in Fig. 8b shows that the Fermi level of the MoO_3/SiO_2 heterojunction is only slightly above the one of free-standing MoO_3, This confirms the smaller amount of injected negative charge carriers and consequently less n-type doping in MoO_3 layer with respect to the case of MoO_3/MoS_2, despite the pronounced reducibility of this oxide, related to its very deep band edges [80].

The situation at the MoO_3/SiO_2 interface, however, changes considerably if a certain amount of charge-donor impurities are trapped therein. Among various charge-donor impurities, sodium has been widely considered due to its ubiquity in any sample subjected to human

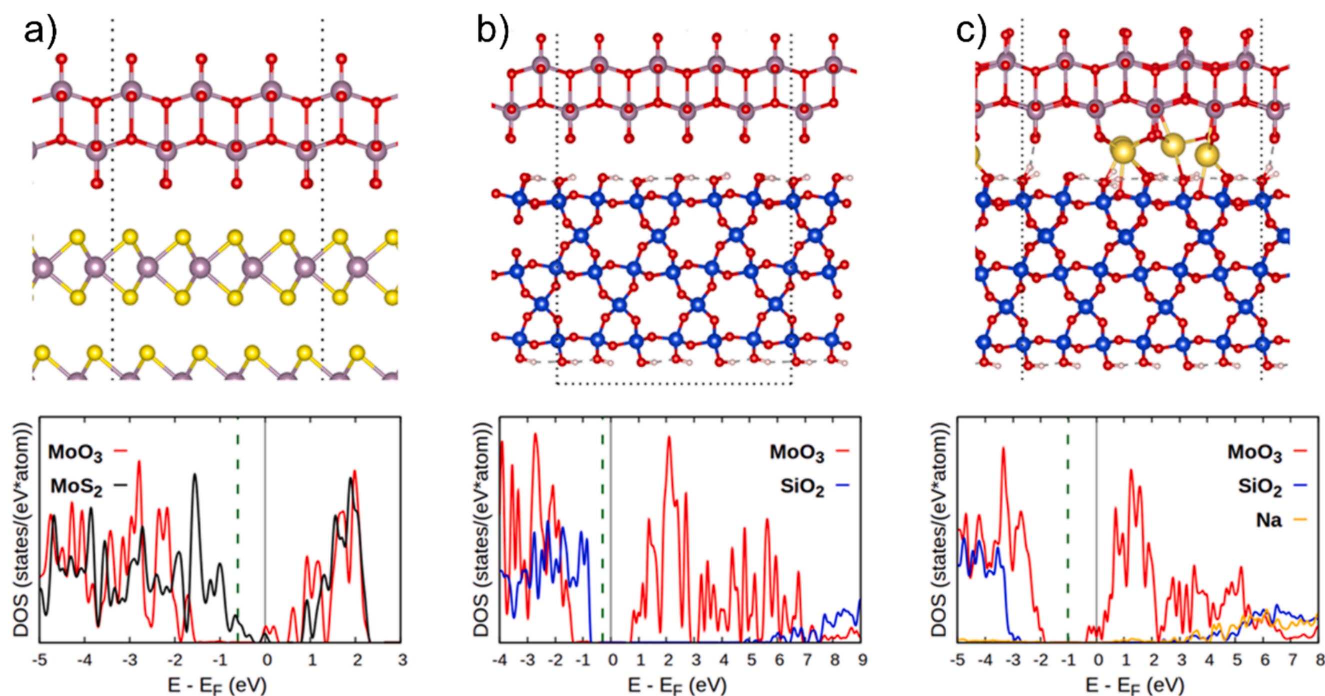

Fig. 8. DFT calculations on heterojunctions. Side views of structures (top) and PDOS plots (bottom) for (a) MoO_3/MoS_2, (b) MoO_3/SiO_2, and (c) MoO_3/Na-doped SiO_2. The zero of the energy scale in the PDOS plot is set at the Fermi level of the heterojunctions. The vertical dashed line represents the Fermi level of free-standing pristine MoO_3.

manipulations [81]. In addition, the Na atoms at the silica surface have been already considered to model the MoS_2/SiO_2 interface and explain its electrical behavior [79]. Sodium atoms atop of the silica slab steadily transfer their electrons to the deepest donor states available, i.e. the conduction band of MoO_3. With a density of Na atoms as large as 1 atom every 16 SiO_2 stoichiometric units, the negative charge transferred to MoO_3 increases to -1.47×10^{14} |e| cm^{-2} (-3.48 |e|/supercell). The PDOS in Fig. 8c shows the charge transfer into the MoO_3 virtual bands, causing a strong upshift of the Fermi level with respect to undoped MoO_3. The quantitative amount of charge transferred into MoO_3 depends on the actual Na concentration, a parameter which can be hardly estimated here.

The charges at the interface between MoO_3 and either of the substrates (SiO_2 or MoS_2) are screened by subsequent MoO_3 layers until the MoO_3 surface potential/work function reach the bulk values. Higher absolute value of $V_{sc}[1]$ obtained for MoO_3 atop MoS_2 than for MoO_3 on SiO_2 suggests stronger electric field therein and consequently more-doped MoO_3 on MoS_2 than on SiO_2. Therefore, it might be a first experimental manifestation of SiO_2-induced MoO_3 doping, because earlier reports concentrated only on oxygen vacancies or heteroatom dopants in MoO_3 as the source of such negative doping [72]. While DFT calculation showed that MoO_3 monolayer receives ca. 20 times more negative charge when it is on a MoS_2 surface than being on a defect-free SiO_2, the absolute value of $V_{sc}[1]$ in the case of MoO_3/MoS_2 is only 1.12 times more than the case of MoO_3/SiO_2. This difference shows that indeed charge impurities such as originating from Na atoms at the MoO_3/SiO_2 play a pivotal role in the MoO_3 doping mechanism.

Lastly, lower K value (screening length) for MoO_3 atop MoS_2 with respect to MoO_3 on SiO_2 can be explained by smaller dielectric constant of Mo oxide structure atop MoS_2. This may be due to its less structured character on MoS_2 than on SiO_2, which was confirmed by our study (Raman and c-AFM).

4. Conclusions

We investigated the work function of thick MoS_2 flakes as well as thickness dependencies of work function of thin MoO_3 layers atop SiO_2 and MoS_2 substrates. In some cases, we also performed detailed high-resolution structural studies. The obtained work function of pristine MoS_2 flakes was 4.85 ± 0.09 eV. In comparison, freshly exfoliated MoS_2 flakes showed slightly higher work function, 4.93 ± 0.16 eV, due to tape residues remained on the surface after mechanical exfoliation. Crystalline MoO_3 flakes on SiO_2 substrates showed increasing work function from 5.03 eV for a monolayer to 5.46 eV for bulk MoO_3. We explained this behavior via presence of an interfacial electric field at the MoO_3/SiO_2 interface. Experimentally we found that the first layer of MoO_3 was negatively charged with potential of −0.428 V. Computationally, we found that electron transfer occurred to MoO_3 from SiO_2 and that it was enhanced in the presence of charge impurities such as Na atoms at the interface. The electric field originating from the transferred charges was screened by subsequent MoO_3 layers with a screening constant of 0.991. Oxidation of MoS_2 in humid environment produced layered amorphous/small crystallite α- or β-MoO_3 oxides. They also showed thickness-dependent WF due to presence of an electric field at the MoO_3/MoS_2 interface caused by an electron transfer from MoS_2 to the oxide. The negative potential at the first layer of oxide was obtained to be −0.480 V, which was screened by subsequent MoO_3 layers with a screening constant of 0.953. Amorphous MoO_3 on MoS_2 had lower electrostatic screening length than crystalline MoO_3 on SiO_2 probably due to lower polarizability of less crystalline MoO_3 onto MoS_2 than in the latter case. The oxide layer also acted as a hole donor to an underlying MoS_2, resulting in a heterostructure, which showed a substantial rectification behavior and other p-n junction characteristics such as low reverse leakage current.

CRediT authorship contribution statement

Saeed Sovizi: Writing – review & editing, Writing – original draft, Visualization, Validation, Methodology, Investigation, Formal analysis, Data curation, Conceptualization. **Sergio Tosoni:** Formal analysis, Methodology, Visualization, Writing – review & editing. **Tomasz Zdunek:** Investigation. **Robert Szoszkiewicz:** Writing – review & editing,

Validation, Supervision, Resources, Project administration, Methodology, Funding acquisition, Formal analysis, Conceptualization.

Declaration of competing interest

The authors declare that they have no known competing financial interests or personal relationships that could have appeared to influence the work reported in this paper.

Data availability

Data will be made available on request.

Acknowledgements

The research has been supported by the National Science Center, Poland, Opus grant no. 2017/27/B/ST4/00697 and partially also by the IDUB grant no BOB-IDUB-622-81/2021 from the Excellence Initiative – Research University (2020-2026) funded by Ministry of Science and Higher Education to the University of Warsaw (UW). We would like to acknowledge Prof. Adam Lewera and Dr Maciej T. Gorzkowski for UPS measurements of the HOPG sample. We thank Dr M. Strawski for help with XPS. The UPS and XPS studies has been carried out in part at the Biological and Chemical Research Centre, UW, established within the project co-financed by European Union from the European Regional Development Fund under the Operational Programme Innovative Economy, 2007-2013. We thank Dr Karol Nogajewski for help with device fabrication within the Lithography Laboratory at Center of New Technologies of UW. We also thank Dr Agata Królikowska for help in Raman measurements and dr Sylwia Turczyniak-Surdacka for SEM measurements. Finally, SS and RSz are also a part of EU COST (European Cooperation in Science and Technology) Action COSY (CA21101).

Appendix A. Supplementary material

Supplementary material to this article can be found online at https://doi.org/10.1016/j.apsusc.2024.160578.

References

[1] Q.H. Wang, K. Kalantar-Zadeh, A. Kis, J.N. Coleman, M.S. Strano, Electronics and optoelectronics of two-dimensional transition metal dichalcogenides, Nat. Nanotechnol. 7 (2012) 699–712, https://doi.org/10.1038/nnano.2012.193.

[2] B. Radisavljevic, A. Radenovic, J. Brivio, V. Giacometti, A. Kis, Single-layer MoS_2 transistors, Nat. Nanotechnol. 6 (2011) 147–150, https://doi.org/10.1038/nnano.2010.279.

[3] S. Sovizi, R. Szoszkiewicz, Single atom doping in 2D layered MoS_2 from a periodic table perspective, Surf. Sci. Rep. 77 (2022) 100567, https://doi.org/10.1016/J.SURFREP.2022.100567.

[4] M.R. Rahmani Taji Boyuk, S. Sovizi, H. Ghanbari, A. Simchi, N. Aboudzadeh, Developing seedless growth of atomically thin semiconductor layers: application to transition metal dichalcogenides, Ceram. Int. 44 (2018) 15795–15803, https://doi.org/10.1016/j.ceramint.2018.05.256.

[5] S. Sovizi, S. Angizi, S.A. Ahmad Alem, R. Goodarzi, M.R.R. Taji Boyuk, H. Ghanbari, R. Szoszkiewicz, A. Simchi, P. Kruse, Plasma processing and treatment of 2D transition metal dichalcogenides: tuning properties and defect engineering, Chem. Rev. 123 (2023) 13869–13951, https://doi.org/10.1021/ACS.CHEMREV.3C00147.

[6] R. Szoszkiewicz, Local interactions of atmospheric oxygen with MoS_2 Crystals, Mater. 14 (2021) 5979, https://doi.org/10.3390/MA14205979.

[7] M. Rogala, S. Sokołowski, U. Ukegbu, A. Mierzwa, R. Szoszkiewicz, Direct identification of surface bound MoO_3 on Single MoS_2 flakes heated in dry and humid air, Adv. Mater. Interf. 8 (2021) 2100328, https://doi.org/10.1002/ADMI.202100328.

[8] Y. Guo, L. Kang, P. Song, Q. Zeng, B. Tang, J. Yang, Y. Wu, D. Tian, M. Xu, W. Zhao, X. Qi, Z. Zhang, Z. Liu, MoO3–MoS2 vertical heterostructures synthesized via one-step CVD process for optoelectronics, 2D Mater. 8 (2021) 035036, https://doi.org/10.1088/2053-1583/ABFEDE.

[9] R. Zhang, X. Ma, C. An, D. Zhang, D. Sun, X. Hu, J. Liu, Self-powered photodetector based on vertical MoO_3/MoS_2 hetero-structure with gate tunable photo-response, 2D Mater. 6 (2019) 035033, https://doi.org/10.1088/2053-1583/AB1CE7.

[10] H. Zhu, X. Qin, L. Cheng, A. Azcatl, J. Kim, R.M. Wallace, Remote plasma oxidation and atomic layer etching of MoS_2, ACS Appl. Mater. Interf. 8 (2016) 19119–19126, https://doi.org/10.1021/ACSAMI.6B04719.

[11] F. Giannazzo, G. Fisichella, G. Greco, S. Di Franco, I. Deretzis, A. La Magna, C. Bongiorno, G. Nicotra, C. Spinella, M. Scopelliti, B. Pignataro, S. Agnello, F. Roccaforte, Ambipolar MoS_2 transistors by nanoscale tailoring of schottky barrier using oxygen plasma functionalization, ACS Appl. Mater. Interf. 9 (2017) 23164–23174, https://doi.org/10.1021/ACSAMI.7B04919.

[12] F. Giannazzo, S.E. Panasci, E. Schilirò, F. Roccaforte, A. Koos, M. Nemeth, B. Pécz, F. Giannazzo, S.E. Panasci, E. Schilirò, F. Roccaforte, A. Koos, M. Nemeth, B. Pécz, Esaki diode behavior in highly uniform mos2/silicon carbide heterojunctions, Adv. Mater. Interf. 9 (2022) 2200915, https://doi.org/10.1002/ADMI.202200915.

[13] F. Giannazzo, S.E. Panasci, E. Schilirò, G. Greco, F. Roccaforte, G. Sfuncia, G. Nicotra, M. Cannas, S. Agnello, E. Frayssinet, Y. Cordier, A. Michon, A. Koos, B. Pécz, Atomic resolution interface structure and vertical current injection in highly uniform MoS_2 heterojunctions with bulk GaN, Appl. Surf. Sci. 631 (2023) 157513, https://doi.org/10.1016/J.APSUSC.2023.157513.

[14] X. Yao, Z. Zhang, L.X. Chen, Z.W. Chen, Y.F. Zhu, C.V. Singh, Work Function-tailored Nitrogenase-like Fe double-atom catalysts on transition metal dichalcogenides for nitrogen fixation, ACS Sustain. Chem. Eng. 11 (2022) 4990–4997, https://doi.org/10.1021/ACSSUSCHEMENG.2C06460.

[15] M. Sharma, J.H. Jang, D.Y. Shin, J.A. Kwon, D.H. Lim, D. Choi, H. Sung, J. Jang, S. Y. Lee, K.Y. Lee, H.Y. Park, N. Jung, S.J. Yoo, Work function-tailored graphene via transition metal encapsulation as a highly active and durable catalyst for the oxygen reduction reaction, Energy Environ. Sci. 12 (2019) 2200–2211, https://doi.org/10.1039/C9EE00381A.

[16] S. Singh, R. Punia, K.K. Pant, P. Biswas, Effect of work-function and morphology of heterostructure components on CO_2 reduction photo-catalytic activity of MoS_2-Cu_2O heterostructure, Chem. Eng. J. 433 (2022) 132709, https://doi.org/10.1016/J.CEJ.2021.132709.

[17] S. Duraisamy, A. Ganguly, P.K. Sharma, J. Benson, J. Davis, P. Papakonstantinou, One-step hydrothermal synthesis of phase-engineered MoS_2/MoO_3 electrocatalysts for hydrogen evolution reaction, ACS Appl. Nano Mater. 4 (2021) 2642–2656, https://doi.org/10.1021/ACSANM.0C03274.

[18] S. Günther, B. Kaulich, L. Gregoratti, M. Kiskinova, Photoelectron microscopy and applications in surface and materials science, Prog. Surf. Sci. 70 (2002) 187–260, https://doi.org/10.1016/S0079-6816(02)00007-2.

[19] J.E. Whitten, Ultraviolet photoelectron spectroscopy: practical aspects and best practices, Appl. Surf. Sci. Adv. 13 (2023) 100384, https://doi.org/10.1016/J.APSADV.2023.100384.

[20] G.F. Rempfer, O.H. Griffith, The resolution of photoelectron microscopes with UV, X-ray, and synchrotron excitation sources, Ultramicroscopy. 27 (1989) 273–300, https://doi.org/10.1016/0304-3991(89)90019-3.

[21] X. Wang, J. Dan, Z. Hu, J.F. Leong, Q. Zhang, Z. Qin, S. Li, J. Lu, S.J. Pennycook, W. Sun, C.H. Sow, Defect heterogeneity in monolayer WS2 unveiled by work function variance, Chem. Mater. 31 (2019) 7970–7978, https://doi.org/10.1021/ACS.CHEMMATER.9B02157.

[22] W. Melitz, J. Shen, A.C. Kummel, S. Lee, Kelvin probe force microscopy and its application, Surf. Sci. Rep. 66 (2011) 1–27, https://doi.org/10.1016/J.SURFREP.2010.10.001.

[23] A. Sohn, H. Moon, J. Kim, M. Seo, K.A. Min, S.W. Lee, S. Yoon, S. Hong, D.W. Kim, Band alignment at Au/MoS_2 Contacts: thickness dependence of exfoliated flakes, J. Phys. Chem. C. 121 (2017) 22517–22522, https://doi.org/10.1021/ACS.JPCC.7B07511.

[24] C. Lattyak, K. Gehrke, M. Vehse, Layer-thickness-dependent work function of MoS2 on metal and metal oxide substrates, J. Phys. Chem. C. 126 (2022) 13929–13935, https://doi.org/10.1021/ACS.JPCC.2C03268.

[25] J.F. Curry, T. Ohta, F.W. DelRio, P. Mantos, M.R. Jones, T.F. Babuska, N.S. Bobbitt, N. Argibay, B.A. Krick, M.T. Dugger, M. Chandross, Structurally driven environmental degradation of friction in MoS_2 films, Tribol. Lett. 69 (2021) 1–10, https://doi.org/10.1007/S11249-021-01453-7.

[26] S.H. Choi, Z. Shaolin, W. Yang, Layer-number-dependent work function of MoS_2 nanoflakes, J. Korean Phys. Soc. 6410 (64) (2014) 1550–1555, https://doi.org/10.3938/JKPS.64.1550.

[27] E. Pollmann, S. Sleziona, T. Foller, U. Hagemann, C. Gorynski, O. Petri, L. Madauß, L. Breuer, M. Schleberger, Large-area, two-dimensional MoS_2 exfoliated on gold: direct experimental access to the metal-semiconductor interface, ACS Omega. 6 (2021) 15929–15939, https://doi.org/10.1021/ACSOMEGA.1C01570.

[28] H.J. Jin, W.Y. Yoon, W. Jo, Control of work function of MoS_2 with ferroelectric polarization in honeycomb-like heterostructure, Appl. Phys. Lett. 110 (2017) 191601, https://doi.org/10.1063/1.4983204/311669.

[29] J.H. Kim, J. Lee, J.H. Kim, C.C. Hwang, C. Lee, J.Y. Park, Work function variation of MoS_2 atomic layers grown with chemical vapor deposition: the effects of thickness and the adsorption of water/oxygen molecules, Appl. Phys. Lett. 106 (2015) 251606, https://doi.org/10.1063/1.4923202/27008.

[30] Y. Li, C.Y. Xu, L. Zhen, Surface potential and interlayer screening effects of few-layer MoS_2 nanoflakes, Appl. Phys. Lett. 102 (2013) 143110, https://doi.org/10.1063/1.4801844/125226.

[31] D.A. Kowalczyk, M. Rogala, K. Szałowski, D. Belić, P. Dąbrowski, P. Krukowski, I. Lutsyk, M. Piskorski, A. Nadolska, P. Krempiński, M. Le Ster, P.J. Kowalczyk, Two-dimensional crystals as a buffer layer for high work function applications: the case of monolayer MoO_3, ACS Appl. Mater. Interf. 14 (2022) 44506–44515, https://doi.org/10.1021/ACSAMI.2C09946.

[32] J.H. Kim, C. Hyun, H. Kim, J.K. Dash, K. Ihm, G.H. Lee, Thickness-insensitive properties of α-MoO_3 nanosheets by weak interlayer coupling, Nano Lett. 19 (2019) 8868–8876, https://doi.org/10.1021/ACS.NANOLETT.9B03701.

[33] H. Irfan, Y. Ding, C. Gao, D.Y. Small, J. Kim, F. Subbiah, So, Energy level evolution of air and oxygen exposed molybdenum trioxide films, Appl. Phys. Lett. 96 (2010) 243307, https://doi.org/10.1063/1.3454779/338896.

[34] J. Meyer, A.L. Kahn, Electronic structure of molybdenum-oxide films and associated charge injection mechanisms in organic devices, J. Photonics Energy 1 (2011) 011109, https://doi.org/10.1117/1.355508.
[35] M.B. Ghasemian, Y. Wang, F.M. Allioux, A. Zavabeti, K. Kalantar-Zadeh, Coating of gallium-based liquid metal particles with molybdenum oxide and oxysulfide for electronic band structure modulation, Nanoscale. 15 (2023) 5891–5898, https://doi.org/10.1039/D2NR06733A.
[36] Y. Wang, M. Mayyas, J. Yang, M.B. Ghasemian, J. Tang, M. Mousavi, J. Han, M. Ahmed, M. Baharfar, G. Mao, Y. Yao, D. Esrafilzadeh, D. Cortie, K. Kalantar-Zadeh, Liquid-metal-assisted deposition and patterning of molybdenum dioxide at low temperature, ACS Appl. Mater. Interf. 13 (2021) 53181–53193, https://doi.org/10.1021/ACSAMI.1C15367.
[37] S. Gupta, A. Johnston, S. Khondaker, Correlated KPFM and TERS imaging to elucidate defect-induced inhomogeneities in oxygen plasma treated 2D MoS_2 nanosheets, J. Appl. Phys. 131 (2022) 164303, https://doi.org/10.1063/5.0088330.
[38] D. Lee, J. Hyuck Jang, W. Song, J. Moon, Y. Kim, J. Lee, B. Jeong, S. Park, In situ work-function measurement during chemical transformation of MoS_2 to MoO_3 by ambient-pressure x-ray photoelectron spectroscopy, 2D Mater. 7 (2020) 025014, https://doi.org/10.1088/2053-1583/AB6780.
[39] A.J. Molina-Mendoza, J.L. Lado, J.O. Island, M.A. Niño, L. Aballe, M. Foerster, F. Y. Bruno, A. López-Moreno, L. Vaquero-Garzon, H.S.J. Van Der Zant, G. Rubio-Bollinger, N. Agraït, E.M. Pérez, J. Fernández-Rossier, A. Castellanos-Gomez, Centimeter-scale synthesis of ultrathin layered MoO_3 by van der Waals Epitaxy, Chem. Mater. 28 (2016) 4042–4051, https://doi.org/10.1021/acs.chemmater.6b01505.
[40] R. Szoszkiewicz, M. Rogala, P. Dąbrowski, Surface-bound and volatile Mo oxides produced during oxidation of single MoS_2 crystals in air and high relative humidity, Mater. 13 (2020) 3067, https://doi.org/10.3390/MA13143067.
[41] N. Fairley, V. Fernandez, M. Richard-Plouet, C. Guillot-Deudon, J. Walton, E. Smith, D. Flahaut, M. Greiner, M. Biesinger, S. Tougaard, D. Morgan, J. Baltrusaitis, Systematic and collaborative approach to problem solving using X-ray photoelectron spectroscopy, Appl. Surf. Sci. Adv. 5 (2021) 100112, https://doi.org/10.1016/J.APSADV.2021.100112.
[42] G. Kresse, J. Hafner, *Ab initio* molecular dynamics for liquid metals, Phys. Rev. B. 47 (1993) 558–561, https://doi.org/10.1103/PhysRevB.47.558.
[43] G. Kresse, J. Furthmüller, Efficient iterative schemes for *ab initio* total-energy calculations using a plane-wave basis set, Phys. Rev. B. 54 (1996) 11169, https://doi.org/10.1103/PhysRevB.54.11169.
[44] P.E. Blöchl, Projector augmented-wave method, Phys. Rev. B. 50 (1994) 17953–17979, https://doi.org/10.1103/PhysRevB.50.17953.
[45] G. Kresse, D. Joubert, From ultrasoft pseudopotentials to the projector augmented-wave method, Phys. Rev. B. 59 (1999) 1758–1775, https://doi.org/10.1103/PhysRevB.59.1758.
[46] J.P. Perdew, K. Burke, M. Ernzerhof, Generalized gradient approximation made simple, Phys. Rev. Lett. 77 (1996) 3865–3868, https://doi.org/10.1103/PhysRevLett.77.3865.
[47] S. Grimme, J. Antony, S. Ehrlich, H. Krieg, A consistent and accurate ab initio parametrization of density functional dispersion correction (DFT-D) for the 94 elements H-Pu, J. Chem. Phys. 132 (2010), https://doi.org/10.1063/1.3382344.
[48] S. Grimme, S. Ehrlich, L. Goerigk, Effect of the damping function in dispersion corrected density functional theory, J. Comput. Chem. 32 (2011) 1456–1465, https://doi.org/10.1002/jcc.21759.
[49] R.F.W. Bader, A quantum theory of molecular structure and its applications, Chem. Rev. 91 (1991) 893–928, https://doi.org/10.1021/CR00005A013/ASSET/CR00005A013.FP.PNG_V03.
[50] G. Henkelman, A. Arnaldsson, H. Jónsson, A fast and robust algorithm for Bader decomposition of charge density, Comput. Mater. Sci. 36 (2006) 354–360, https://doi.org/10.1016/J.COMMATSCI.2005.04.010.
[51] C. Freysoldt, J. Neugebauer, First-principles calculations for charged defects at surfaces, interfaces, and two-dimensional materials in the presence of electric fields, Phys. Rev. B. 97 (2018) 205425, https://doi.org/10.1103/PHYSREVB.97.205425.
[52] W.N. Hansen, G.J. Hansen, Standard reference surfaces for work function measurements in air, Surf. Sci. 481 (2001) 172–184, https://doi.org/10.1016/S0039-6028(01)01036-6.
[53] U. Ukegbu, R. Szoszkiewicz, Microscopic kinetics of heat-induced oxidative etching of thick MoS_2 crystals, J. Phys. Chem. C. 123 (2019) 22123–22129, https://doi.org/10.1021/ACS.JPCC.9B02739.
[54] S. Sovizi, S. Tosoni, R. Szoszkiewicz, MoS_2 oxidative etching caught in the act: formation of single (MoO_3) n molecules, Nanoscale Adv. 4 (2022) 4517–4525, https://doi.org/10.1039/D2NA00374K.
[55] I. Irfan, A. James Turinske, Z. Bao, Y. Gao, Work function recovery of air exposed molybdenum oxide thin films, Appl. Phys. Lett. 101 (2012) 93305, https://doi.org/10.1063/1.4748978/111730.
[56] J. Liu, S. Shao, G. Fang, B. Meng, Z. Xie, L. Wang, High-efficiency inverted polymer solar cells with transparent and work-function tunable MoO3-Al composite film as cathode buffer layer, Adv. Mater. 24 (2012) 2774–2779, https://doi.org/10.1002/ADMA.201200238.
[57] L. Seguin, M. Figlarz, R. Cavagnat, J.C. Lassègues, Infrared and Raman spectra of MoO_3 molybdenum trioxides and $MoO_3 \cdot xH_2O$ molybdenum trioxide hydrates, Spectrochim Acta Part A Mol. Biomol. Spectrosc. 51 (1995) 1323–1344, https://doi.org/10.1016/0584-8539(94)00247-9.
[58] M.A. Camacho-López, L. Escobar-Alarcón, M. Picquart, R. Arroyo, G. Córdoba, E. Haro-Poniatowski, Micro-Raman study of the m-MoO_2 to α-MoO_3 transformation induced by cw-laser irradiation, Opt. Mater. (Amst) 33 (2011) 480–484, https://doi.org/10.1016/J.OPTMAT.2010.10.028.
[59] A. Castellanos-Gomez, E. Cappelluti, R. Roldán, N. Agraït, F. Guinea, G. Rubio-Bollinger, A. Castellanos-Gomez, E. Cappelluti, R. Roldán, F. Guinea, N. Agraït, G. Rubio-Bollinger, Electric-field screening in atomically thin layers of MoS_2: the role of interlayer coupling, Adv. Mater. 25 (2013) 899–903, https://doi.org/10.1002/ADMA.201203731.
[60] F. Li, J. Qi, M. Xu, J. Xiao, Y. Xu, X. Zhang, S. Liu, Y. Zhang, Layer dependence and light tuning surface potential of 2D MoS_2 on various substrates, Small. 13 (2017) 1603103, https://doi.org/10.1002/SMLL.201603103.
[61] S. Das, J. Appenzeller, Screening and interlayer coupling in multilayer MoS_2, Phys. Status Solidi – Rapid Res Lett. 7 (2013) 268–273, https://doi.org/10.1002/PSSR.201307015.
[62] R. He, H. Lai, S. Wang, T. Chen, F. Xie, Q. Chen, P. Liu, J. Chen, W. Xie, Few-layered vdW MoO_3 for sensitive, uniform and stable SERS applications, Appl. Surf. Sci. 507 (2020) 145116, https://doi.org/10.1016/J.APSUSC.2019.145116.
[63] B.A. Holler, K. Crowley, M.H. Berger, X.P.A. Gao, 2D Semiconductor Transistors with Van der Waals Oxide MoO_3 as Integrated High-κ Gate Dielectric, Adv. Electron. Mater. 6 (2020) 2000635, https://doi.org/10.1002/AELM.202000635.
[64] Y. Hou, G. Wang, C. Ma, Z. Feng, Y. Chen, T. Filleter, Quantification of the dielectric constant of MoS_2 and WSe_2 Nanosheets by electrostatic force microscopy, Mater. Charact. 193 (2022) 112313, https://doi.org/10.1016/J.MATCHAR.2022.112313.
[65] M. Belete, S. Kataria, U. Koch, M. Kruth, C. Engelhard, J. Mayer, O. Engström, M. C. Lemme, Dielectric properties and ion transport in layered MoS_2 grown by vapor-phase sulfurization for potential applications in nanoelectronics, ACS Appl. Nano Mater. 1 (2018) 6197–6204, https://doi.org/10.1021/ACSANM.8B01412.
[66] P. Atkin, D.W.M. Lau, Q. Zhang, C. Zheng, K.J. Berean, M.R. Field, J.Z. Ou, I. S. Cole, T. Daeneke, K. Kalantar-Zadeh, Laser exposure induced alteration of WS2 monolayers in the presence of ambient moisture, 2D Mater. 5 (2017) 015013, https://doi.org/10.1088/2053-1583/AA91B8.
[67] S.A. Sumaiya, J. Liu, M.Z. Baykara, True atomic-resolution surface imaging and manipulation under ambient conditions via conductive atomic force microscopy, ACS Nano. 16 (2022) 20086–20093, https://doi.org/10.1021/ACSNANO.2C08321.
[68] F. Bertoldo, S. Canulescu, R.R. Unocic, Y.C. Lin, X. Sang, A.A. Puretzky, Y. Yu, D. Miakota, C.M. Rouleau, J. Schou, K.S. Thygesen, D.B. Geohegan, Intrinsic defects in MoS_2 grown by pulsed laser deposition: from monolayers to bilayers, ACS Nano. 15 (2021) 2858–2868, https://doi.org/10.1021/ACSNANO.0C08835.
[69] J. Wang, R. Namburu, M. Dubey, A.M. Dongare, Origins of Moiré Patterns in CVD-grown MoS2 Bilayer Structures at the Atomic Scales, Sci. Reports 2018 81. 8 (2018) 1–9. 10.1038/s41598-018-27582-z.
[70] M.L. Lin, Q.H. Tan, J. Bin Wu, X.S. Chen, J.H. Wang, Y.H. Pan, X. Zhang, X. Cong, J. Zhang, W. Ji, P.A. Hu, K.H. Liu, P.H. Tan, Moiré phonons in twisted bilayer MoS_2, ACS Nano. 12 (2018) 8770–8780, https://doi.org/10.1021/ACSNANO.8B05006.
[71] A. Yoon, J.H. Kim, J. Yoon, Y. Lee, Z. Lee, van der Waals epitaxial formation of atomic layered α-MoO_3 on MoS_2 by oxidation, ACS Appl. Mater. Interf. 12 (2020) 22029–22036, https://doi.org/10.1021/ACSAMI.0C03032.
[72] I. Alves de Castro, R. Shankar Datta, J. Zhen Ou, A. Castellanos-Gomez, S. Sriram, T. Daeneke, K. Kalantar-zadeh, Molybdenum oxides – from fundamentals to functionality, Adv. Mater. 29 (2017) 1701619, https://doi.org/10.1002/ADMA.201701619.
[73] Y. Zhang, X. Ping, L. Hao, Y. He, Y. Guo, Q. Zhao, Z. Zheng, Y. Lu, Facile preparation of anodized MoO_{3-x} films and their boosted photocatalytic activity, J. Environ. Chem. Eng. 9 (2021) 105565, https://doi.org/10.1016/J.JECE.2021.105565.
[74] B. Li, L. Jiang, X. Li, P. Ran, P. Zuo, A. Wang, L. Qu, Y. Zhao, Z. Cheng, Y. Lu, Preparation of monolayer MoS_2 quantum dots using temporally shaped femtosecond laser ablation of bulk MoS_2 targets in water, Sci. Rep. 71 (7) (2017) 1–12, https://doi.org/10.1038/s41598-017-10632-3.
[75] X. Zheng, A. Calò, E. Albisetti, X. Liu, A.S.M. Alharbi, G. Arefe, X. Liu, M. Spieser, W.J. Yoo, T. Taniguchi, K. Watanabe, C. Aruta, A. Ciarrocchi, A. Kis, B.S. Lee, M. Lipson, J. Hone, D. Shahrjerdi, E. Riedo, Patterning metal contacts on monolayer MoS_2 with vanishing Schottky barriers using thermal nanolithography, Nat. Electron. 21 (2) (2019) 17–25, https://doi.org/10.1038/s41928-018-0191-0.
[76] K. Choi, S.R.A. Raza, H.S. Lee, P.J. Jeon, A. Pezeshki, S.W. Min, J.S. Kim, W. Yoon, S.Y. Ju, K. Lee, S. Im, Trap density probing on top-gate MoS_2 nanosheet field-effect transistors by photo-excited charge collection spectroscopy, Nanoscale. 7 (2015) 5617–5623, https://doi.org/10.1039/C4NR06707J.
[77] K.K.H. Smithe, S.V. Suryavanshi, M. Muñoz Rojo, A.D. Tedjarati, E. Pop, Low variability in synthetic monolayer MoS_2 devices, ACS Nano. 11 (2017) 8456–8463, https://doi.org/10.1021/ACSNANO.7B04100/ASSET.
[78] Z. Gao, Z. Zhou, D. Tománek, Degenerately doped transition metal dichalcogenides as ohmic homojunction contacts to transition metal dichalcogenide semiconductors, ACS Nano. 13 (2019) 5103–5111, https://doi.org/10.1021/ACSNANO.8B08190.
[79] K. Dolui, I. Rungger, S. Sanvito, Origin of the n-type and p-type conductivity of MoS_2 monolayers on a SiO_2 substrate, Phys. Rev. B - Condens. Matter Mater. Phys. 87 (2013) 165402, https://doi.org/10.1103/PHYSREVB.87.165402.
[80] Y. Guo, J. Robertson, Origin of the high work function and high conductivity of MoO_3, Appl. Phys. Lett. 105 (2014) 222110, https://doi.org/10.1063/1.4903538/132898.
[81] H. Habuka, K. Suzuki, S. Okamura al, A. Rezka Putra, G. Setiawan, Deposition and removal of sodium contamination on silicon wafers, Semicond. Sci. Technol. 15 (2000) 61, https://doi.org/10.1088/0268-1242/15/1/311.